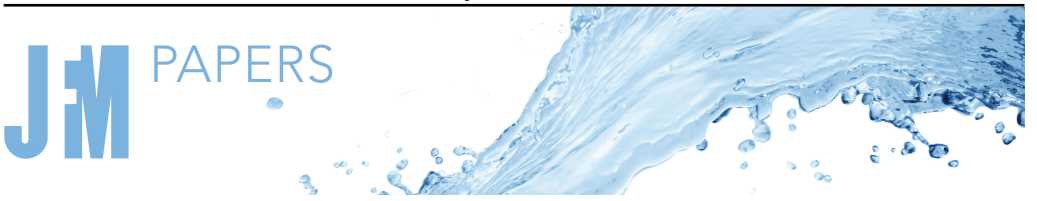
J. Fluid Mech. (2025), *vol.* 1022, A31, doi:10.1017/jfm.2025.10813



Experimental study of diffusiophoresis in a cellular flow

Florence Raynal[1], **Menghua Zhao**[1,2] **and Romain Volk**[2]

[1]Laboratoire de Mécanique des Fluides et d'Acoustique, CNRS UMR 5509, École centrale de Lyon, INSA Lyon, Université Claude Bernard Lyon 1, Écully CÉDEX 69134, France

[2]Laboratoire de Physique, ENS de Lyon, CNRS, Lyon F-69342, France

Corresponding author: Florence Raynal, florence.raynal@ec-lyon.fr

(Received 2 December 2024; revised 17 September 2025; accepted 24 September 2025)

In this paper, we study experimentally the dispersion of colloids in a two-dimensional, time-independent, Rayleigh–Bénard flow in the presence of salt gradients. Due to the additional scalar, the colloids do not follow exactly the Eulerian flow field, but have a (small) extra velocity $\boldsymbol{v}_{dp} = D_{dp}\,\boldsymbol{\nabla}\log C_s$, where D_{dp} is the phoretic constant, and C_s is the salt concentration. Such a configuration is motivated by the theoretical work by Volk *et al.* (2022, *J. Fluid Mech.*, vol. 948, A42), which predicted enhanced transport or blockage in a stationary cellular flow depending on the value of a blockage coefficient. By means of high dynamical range light-induced fluorescence, we study the evolution of the colloids concentration field at large Péclet number. We find good agreement with the theoretical work, although a number of hypotheses are not satisfied, as the experiment is non-homogeneous in space, and intrinsically transient. In particular, we observe enhanced transport when salt and colloids are injected at both ends of the Rayleigh–Bénard chamber, and blockage when colloids and salt are injected together and phoretic effects are strong enough.

Key words: colloids, active matter, dispersion

1. Introduction

The transport of particles or macro-molecules in a flow can be affected by concentration gradients of a scalar field present in the flow, such as temperature, solute concentration or nutrient in the case of living organisms. Such phoretic particles do not follow exactly the Eulerian flow field, but have a small drift velocity, the precise expression for which depends on the physical phenomenon involved. In the case of charged colloids in water, this extra displacement is related to electrokinetic effects, and the phenomenon is called diffusiophoresis: due to salt gradients, the drift velocity takes the form $\boldsymbol{v}_{dp} = D_{dp}\,\boldsymbol{\nabla}\log C_s$, where D_{dp} is the diffusiophoretic mobility, and C_s is the salt concentration

© The Author(s), 2025. Published by Cambridge University Press.

https://doi.org/10.1017/jfm.2025.10813 Published online by Cambridge University Press

(Derjaguin, Dukhin & Korotkova 1961; Prieve *et al.* 1984; Anderson 1989; Ault & Shin 2025).

Although the drift velocity is usually very small compared to any macroscopic fluid velocity, it has a strong influence on how the phoretic particles spread inside the flow, even at the macro-scale (Mauger *et al.* 2016). In particular, it was found that mixing could be delayed or enhanced depending on if the colloids are introduced together with the salt or introduced in salted water: for instance, Abécassis *et al.* (2009) showed in a Ψ-channel that the diffusiophoretic effect could be modelled by a diffusive behaviour, with a positive or negative effective diffusion coefficient much greater than that of the large colloidal particle; in chaotic advection, mixing of colloids was measured using an effective Péclet number (Deseigne *et al.* 2014; Mauger *et al.* 2016; Raynal & Volk 2019). However, the complex behaviour of colloidal particles cannot be summed up by a simple diffusive effect; indeed, its origin lies in the compressibility of the drift velocity $\boldsymbol{\nabla \cdot v}_{dp}$, which can be set to be positive or negative depending on the configuration (Volk *et al.* 2014; Raynal *et al.* 2018; Renaud & Vanneste 2020; Chu *et al.* 2020, 2021, 2022).

Another important situation, often encountered in practical applications and distinct from the previous open flows above, is the case of flows with closed streamlines. Indeed, most flows have recirculation loops from which a perfect tracer cannot escape if the flow remains steady. In particular, the transport of a passive scalar in an array of vortices with closed streamlines was the focus of several theoretical and experimental studies (Shraiman 1987; Soward 1987; Young, Pumir & Pomeau 1989; Solomon & Gollub 1988*b*).

In such a configuration, it has been shown that advection–diffusion of Brownian particles leads to diffusive dynamics at long times, with a ratio of their effective diffusivity to the molecular diffusivity growing as the square root of the Péclet number $Pe = UL/D$, where U is the velocity scale, L is the size of the recirculation cell, and D is the molecular diffusivity of the particles. More recently, this study has been extended to the theoretical case of joint transport of salt and phoretic particles (Volk *et al.* 2022). In this work, salt inhomogeneities are forced by a constant salt gradient $\boldsymbol{G}$, leading to strong salt variations in between vortices; phoretic particles have a linear drift velocity of the form $\boldsymbol{v}_{drift} = \alpha\, \boldsymbol{\nabla} C_s$, and are initially homogeneously released. By means of numerical simulations performed in both Eulerian and Lagrangian frameworks, in the limit of realistic large Péclet numbers for both salt and colloids, the authors could address how colloids move or regroup in the flow under the action of advection, diffusion and phoresis. The study showed the existence of two regimes, both very different from the diffusive-like behaviour observed in previous studies, depending on the value of a parameter $R = \alpha G L/(2\sqrt{D_c D_s})$, where D_s and D_c are the diffusion coefficients of salt and colloids, respectively.

(i) For $R \ll 1$, the transport of colloids was strongly enhanced, leading to a mean velocity $v_m \sim \alpha G \sqrt{Pe_s}$, where $Pe_s = UL/D_s$ is the salt Péclet number; this velocity is much larger than the phoretic velocity αG that the particles would have in the absence of flow. This regime is called 'enhanced transport' in the following.

(ii) For $R \gg 1$, when phoretic effects are very strong compared to diffusion, instead of moving even more rapidly in the direction of the mean salt gradient, the colloids are trapped in their cells. This regime is referred to as 'blockage' in the following, and R is called the 'blockage coefficient'.

However, these theoretical findings were obtained in the stationary regime with periodic boundary conditions and a mean salt gradient constant in space, so that phoretic effects could build up in time without any constraint. One may then wonder if these two regimes can be observed experimentally after injection of salt and colloids in some

https://doi.org/10.1017/jfm.2025.10813 Published online by Cambridge University Press

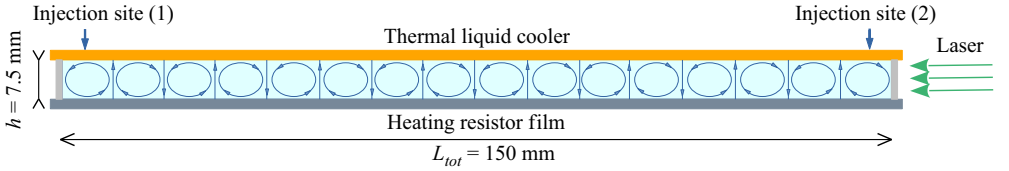


Figure 1. The flow in the Rayleigh–Bénard cell (with length $L_{tot} = 150$ mm, height $h = 7.5$ mm, width $w = 15$ mm) is set above the onset of the first instability and below the second instability using a heating thermal Kapton heater at the bottom and a liquid cooler at the top. Two injection sites are located on each side of the cell. The vertical walls are made of transparent acrylic glass. The fluorescent species (whether colloids or fluorescein) is injected through site (1), and its dispersion is followed using a laser sheet.

bounded convective flow, a problem of dispersion that is intrinsically transient and non-homogeneous in space.

In this paper, we propose to prove experimentally the existence of the two regimes of enhanced transport and blockage. To this end, we use the same phoretic particles as in Mauger *et al.* (2016), i.e. charged colloids that are attracted towards regions of high salt concentration. This makes it impossible to create the cellular flow by electroconvection (Bergougnoux *et al.* 2014) as it would require already salted water, which could screen the diffusiophoretic effects. Rather, we use the experimental configuration of Solomon & Gollub (1988*b*), which takes place in a long horizontal Rayleigh–Bénard cell, where the flow is time-independent and composed of an alignment of steady convection rolls in the closed chamber; see figure 1. In order to study how the injected colloids or salt spread inside the chamber, we follow their instantaneous concentration field using high dynamical range light-induced fluorescence (HDR LIF). We compare our experimental findings with the theory, and recover the two regimes, in particular the counterintuitive regime of blockage.

The paper is organised as follows. In § 2, we describe the experimental set-up and the flow inside the cell; we also detail the multi-exposure times technique used to build the HDR images obtained by LIF, and explain how this was corrected to account for the attenuation of laser light when converting recorded images into concentration fields. In § 3, we characterise the transport of a single species in the flow. We start with fluorescein, whose diffusion coefficient is close to that of salt, and extend these results to salt, whose concentration field is required to apply our theoretical results. Then we study the case of transport of colloids in the absence of salt, therefore without phoretic effects, in order to get a reference for comparison with cases where salt is present. Section 4 is devoted to the phoretic cases, when both colloids and salt are present in the flow. We consider two configurations, one where colloids and salt are injected on the two sides of the chamber (salt-out configuration), the other where colloids and salt are injected together on one side of the chamber (salt-in configuration). We first summarise the theoretical results obtained in Volk *et al.* (2022), in order to transpose them to the experiment afterwards. We then discuss how the regimes of enhanced transport and blockage are obtained. Finally, in the last section, we conclude and summarise the work.

2. Experimental set-up

Mixing takes place in an elongated Rayleigh–Bénard (RB) cell whose geometry is identical to that of Solomon & Gollub (1988*b*). Its horizontal dimensions are $L_{tot} = 15$ cm and $w = 1.5$ cm, and its height is $h = 0.75$ cm, as shown in figure 1. The vertical walls of the chamber are made of transparent acrylic glass in order to perform optical

https://doi.org/10.1017/jfm.2025.10813 Published online by Cambridge University Press

measurements, while the top and bottom covers are composed of brass to ensure a good thermal contact with the fluid.

For concentration measurements, we operate with fluorescent species: fluorescein, whose diffusion coefficient is close to that of the salt used for diffusiophoretic effects (LiCl), and fluorescent colloids, carboxilate microspheres (Invitrogen) of diameter 0.2 μm already used in Mauger *et al.* (2016). The colloids are isodense particles, with negligible inertia. The fluorescent species is introduced through injection hole (1), opposite the laser.

The local concentration of a generic fluorescent species is hereinafter referred to as $C(x, y, t)$. Because we are mostly interested in the spreading in the x-direction, for simplicity we extend the notation C for y-averaged concentration profiles, i.e. $C(x, t) = (1/h) \int_{y=0}^{y=h} C(x, y, t)\, \mathrm{d}y$.

2.1. *Flow characterisation*

In order to generate a convective flow, we create a temperature difference between the top and bottom: a fixed temperature $T = 26\,^{\circ}\mathrm{C}$ is imposed on the top cover with water circulation and a thermal bath, and we set the heat flux through the chamber using a thin 7.5 W Kapton heater placed under the bottom cover. The heating resistive sheet, which is connected to a DC supply, is compressed between the bottom part and an (insulating) PVC block to ensure that most of the heat flux is directed towards the liquid. In order to tune the temperature difference, and more especially set the bottom temperature, top and bottom temperatures are monitored using a picolog acquisition card connected to 4 k-type thermocouples inserted in the top and bottom, in close contact with the fluid. Such thermal driving ensured fine tuning of the temperature difference $\Delta T \in [0.9, 1.5]\,^{\circ}\mathrm{C}$ between top and bottom with good stability. Finally, the whole set-up is placed in a temperature-regulated room to increase the thermal stability of the set-up, which is required since the measurements of mixing last approximately 10 hours.

For all experiments, we use pre-boiled distilled water to either fill the chamber or prepare the salt/colloidal solutions so as to prevent the formation of air bubbles during the long heating of the RB chamber. When operating, the chamber is filled with liquid using two holes drilled on the top cover connected to syringe pumps. When injecting dye or colloids, the injection rate is set to be less than $20\ \mu\mathrm{l\ min}^{-1}$ to avoid any strong perturbation of the convection flow. During an injection process, the lid of the opposite injection site is kept open so as to allow excess water to escape.

For such thermal forcing, the flow regime is controlled by the Rayleigh number $Ra = \gamma g\, \Delta T\, h^3/(\kappa \nu)$, where γ is the thermal expansion of water, g is gravity, κ is thermal diffusivity, and ν is kinematic viscosity of the fluid. The flow is found to be convective when Ra is larger than the critical value $Ra_{cr} = 1708$. In the present case where $h = 0.75$ cm and the fluid is water, this gives $Ra/Ra_{cr} \approx C\, \Delta T$, where $C = 9.2\ \mathrm{K}^{-1}$. Given the range of temperature difference, the set-up is expected to produce steady laminar flows as the threshold for the first bifurcation towards a time-dependent flow corresponds to $Ra/Ra_c \approx 18$ (Solomon & Gollub 1988*a*).

This was verified by performing particle image velocimetry (PIV) measurements of the flow field for increasing values of the temperature difference ΔT. To achieve this, we use a CW laser (Coherent Genesis MX SLM-Series, 1W@488 nm), a cylindrical lens and a 250 μm slit to form a thin vertical laser sheet in the middle of the RB chamber (see figure 1); the flow is seeded with 10 μm silver-coated hollow glass spheres from Dantec. Images are then recorded at 10 fps using an XIMEA camera, and we perform the correlation of pairs of images using a home-made software written in Matlab. The result for the velocity magnitude, averaged in time over 1 minute, is shown in figure 2(*a*),

https://doi.org/10.1017/jfm.2025.10813 Published online by Cambridge University Press

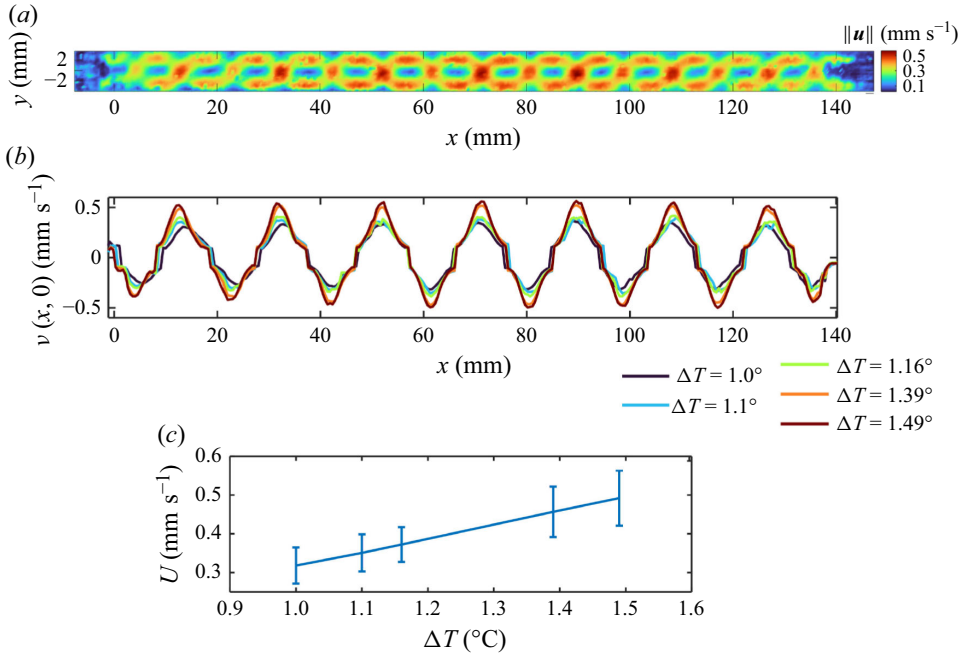


Figure 2. (*a*) Magnitude $\|\boldsymbol{u}\|$ of the velocity field measured by PIV for $\Delta T = 1.37\,°\text{C}$. (*b*) Vertical velocity profile along the centreline inside the RB chamber for several values of the temperature difference ΔT, from 1.00 °C to 1.49 °C. (*c*) Maximum of the velocity magnitude U as a function of ΔT.

where the typical signature of well-organised convection rolls is visible. As shown in figure 2(*b*), which displays a horizontal profile of the vertical velocity at mid-depth of the cell, the spatial organisation of the flow remains the same for all values of ΔT in the range [1, 1.5] °C, and consists of approximately 16 counter-rotating rolls with width $L \approx 9.4$ mm, whose positions are pinched within the chamber.

In the case of RB flow, the bifurcation is of the Hopf type, meaning that the maximum vertical velocity, denoted by U, is such that $U \propto \sqrt{\Delta T - \Delta T_{cr}}$ close to the threshold, where ΔT_{cr} is the top–bottom temperature difference at the threshold. Here, we operate quite far from the threshold, with a limited range of accessible values of the Rayleigh number, so that the flow amplitude rather tends to increase linearly with the temperature difference (figure 2*c*). By fitting linearly the averaged value of U as a function of ΔT, we find $U = 0.36 \times \Delta T - 0.04\,\text{mm s}^{-1}$, so the Reynolds number of the flow based on the chamber height ($Re = Uh/\nu$, where $\nu = 10^{-6}\,\text{m}^2\,\text{s}^{-1}$ is the kinematic viscosity of water) is such that $2.5 \leqslant Re \leqslant 4.5$ for all experiments.

2.2. *Multiple time exposure concentration field measurements*

When a chemical species is injected on one side of the chamber, it is advected and diffused through the convection rolls. Such a mixing process in a steady and well-organised flow is rather inefficient, so that the concentration field spans an HDR during the whole run, with large concentration differences and strong concentration gradients located near separatrixes (Solomon & Gollub 1988*b*). It is therefore very hard to perform direct optical measurements of such a concentration field, even with a high-quality camera. For that purpose, we use a variant of the set-up described in Mauger *et al.* (2016), and perform planar LIF measurements using a multiple time exposure technique.

https://doi.org/10.1017/jfm.2025.10813 Published online by Cambridge University Press

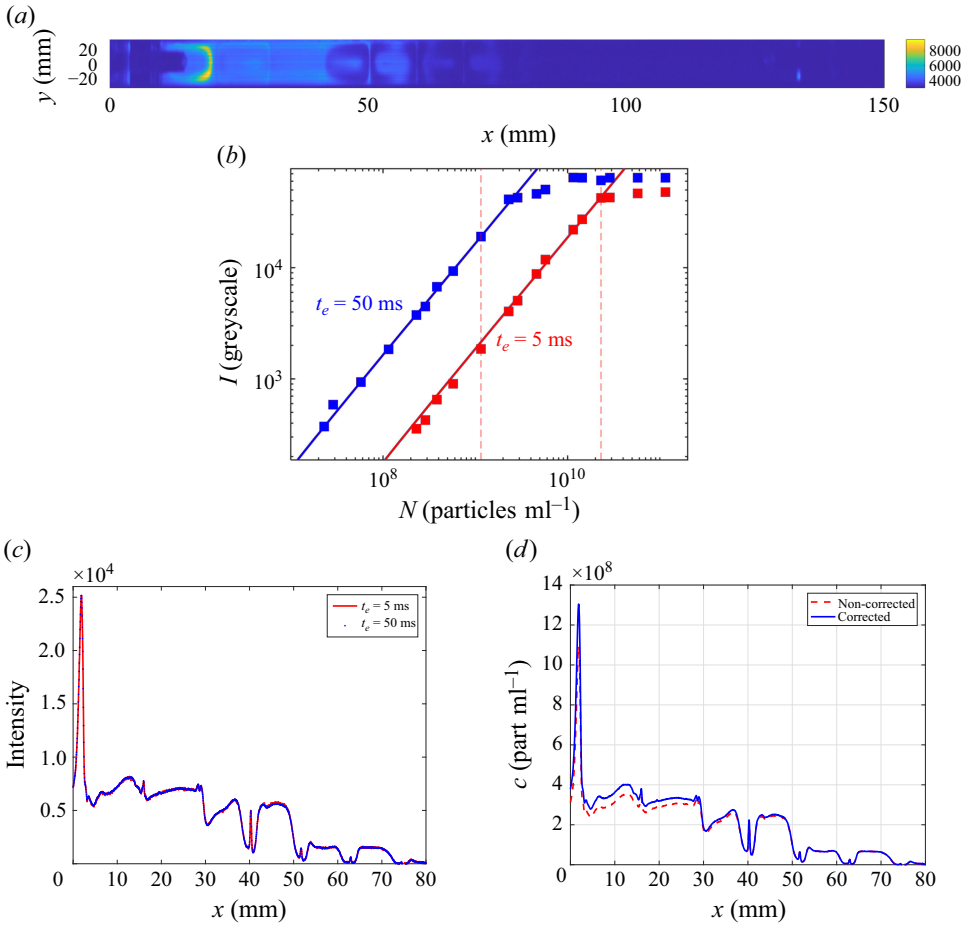


Figure 3. (*a*) Raw image obtained using the LIF set-up and exposure time $t_e = 50$ ms, 10 h after colloid injection. (*b*) Camera calibration curves: squares record intensity measured with increasing homogeneous fluorescein concentration in 2.5 ml cuvettes for two exposure times, $t_e = 5$ and 50 ms. The straight lines correspond to linear fits derived in the linear range $I \leqslant 44\,000$ (60 % of the dynamical range). (*c*) Comparison of x-profiles of recorded intensity averaged over the vertical coordinate y and two exposure times. Blue dots show raw intensity profile measured with $t_e = 50$ ms. The red line shows intensity profile measured with $t_e = 5$ ms, transformed using the linear transformation $\mathcal{T}[I] = \gamma I + \kappa$, with $\gamma = 10.2$ and $\kappa = -951$. (*d*) The x-profiles of concentration averaged over the vertical coordinate y built using the HDR procedure and calibration curves obtained in the chamber with known (homogeneous) colloid concentration. The dashed red line indicates without correction for exponential attenuation through the chamber. The blue solid line indicates with compensation for exponential attenuation.

We use the same optical set-up as for the PIV measurements to create the laser sheet, with almost homogeneous light intensity in the chamber. The fluorescence signal is recorded using a 16-bit camera (Nikon D700, 4200×2800 pixels^2) equipped with a TAMRON 90 mm macro lens and a band reject filter (notch 488 ± 12 nm) corresponding to the laser wavelength. For all experiments, the laser power is set to 195 mW, and the ISO sensitivity is set to its lowest value to avoid noise. After recording, images are cropped to fit the aspect ratio of the cell so that their actual size is 3249×181 pixels^2 in the x- and y-directions, with spatial resolution approximately 44 µm. A typical raw image recorded with exposure time $t_e = 50$ ms several hours after colloid injection on the left-hand side injection site (1) is displayed in figure 3(*a*).

https://doi.org/10.1017/jfm.2025.10813 Published online by Cambridge University Press

2.2.1. *Camera calibration*

In order to calibrate the set-up, one has to relate the recorded intensity on raw images to the local concentration. This was done by using an ensemble of solutions obtained by dilution in 2.5 ml cuvettes, with known fluorescein or colloid concentration. For each solution, we have recorded images for various exposure times in the range $t_e \leqslant 500$ ms in order to check for the linearity of the measurement. The result for the colloids and $t_e = 5$ ms and $t_e = 50$ ms is displayed in figure 3(*b*): the response of the camera is found to be linear when the grey level is smaller than 44 000, which is approximately two-thirds of its total dynamical range (2^{16}). When operating at low enough intensity, we could verify that the measured intensity is linear in colloid concentration (solid lines in figure 3*b*), laser power, and exposure time, as expected for a CMOS camera (Wang 2018).

2.2.2. *The HDR measurement*

Mixing lasts approximately 10–20 hours in the RB chamber, so we use two exposure times, 5 ms and $\tau_2 = 50$ ms, and record pairs of images every 100 seconds; we then build an HDR image from both measurements. To do this, we use the linear transformation $\mathcal{T}[I] = \gamma I + \kappa$, such that $I_{50}(x, y) = \mathcal{T}[I_5(x, y)]$, linking both intensities measured with the two exposure times. Indeed, using such a relation, one can superimpose horizontal intensity profiles obtained from I_{50} and $\mathcal{T}[I_5]$ in the linear regime as shown in figure 3(*c*). (From the data, we obtain $\gamma = 10.2$, which is very close to the ratio between the two exposure times, and $\kappa = -951$, which depends on the electronic offsets of the camera at $t_e = 50$ ms and $t_e = 5$ ms, since the exposure times are switched after performing a black reference prior to the experiment.)

Potential nonlinearities can be eliminated by defining an HDR image as $I_{HDR}(x, y) = I_{50}(x, y)$ everywhere where I_{50} is smaller than 60 % of the sensor dynamical range, and $I_{HDR}(x, y) = \mathcal{T}[I_5(x, y)]$ in any other location. This ensures that we have a low level of noise in the measurement, while using the whole dynamical range of the camera sensor.

Note that the choices of the threshold and values of t_e have a weak impact on the final result, but the present choices are a good compromise given the laser power and typical maximal colloid concentration in the chamber. After combining both raw images taken with two exposure times to build a HDR image, we get rid of ambient illumination by subtracting a background reference image taken with the laser off before starting the experiment. We finally transform these HDR images into concentration fields using concentration–intensity calibration curves while taking into account absorption of light in the chamber, as explained in the next subsubsection.

2.2.3. *Compensation for spatial decay of incoming light*

Given the low concentrations of fluorescent species C used here, the light intensity scattered per unit volume of fluid in the laser sheet is proportional to the local concentration $I_{scat}(x, y, t) = \sigma \times C(x, y, t) \times I_0(x, y, t)$, where σ is a constant specific to the colloids, and $I_0(x, y, t)$ is the incoming light at location (x, y) and time t. Although the precise values of σ and I_0 are not needed as we will work with normalised quantities in the following, light scattering may affect the measurement due to the spatial decay of incoming light $I_0(x, y, t)$, corresponding to the Beer–Lambert law (Swinehart 1962). In the present case, we inject colloids at the location $x = 0$, and propagate the laser beam from $x = L_{tot}$ towards $x = 0$ so that the local Beer–Lambert law reads

$$\frac{\mathrm{d} \log I_0(x, y, t)}{\mathrm{d}x} = \sigma\, C(x, y, t). \tag{2.1}$$

https://doi.org/10.1017/jfm.2025.10813 Published online by Cambridge University Press

This relation can be integrated from x to L_{tot} to give

$$I_0(x,\, y,\, t) = I_0(L_{tot},\, y,\, t) \times \exp\left(-\sigma \int_x^{L_{tot}} C(x',\, y,\, t)\, \mathrm{d}x'\right), \tag{2.2}$$

where $I_0(L_{tot},\, y,\, t)$ is a constant here as the incoming laser light has an almost homogeneous intensity in the y-direction at $x = L_{tot}$, with a constant amplitude in time. Due to the spatial decay of the laser intensity along the chamber, the recorded intensity I_{HDR} is not simply proportional to the concentration. However, I_{HDR} is still proportional to the scattered light intensity if the concentration field is well resolved spatially with a camera operating in the linear regime. Assuming that this is the case here, we then have

$$I_{HDR}(x,\, y,\, t) = A \times C(x,\, y,\, t) \times \exp\left(-\sigma \int_x^{L_{tot}} C(x',\, y,\, t)\, \mathrm{d}x'\right), \tag{2.3}$$

where A is a multiplicative constant.

To recover an unbiased estimate of the concentration field, it is important to accurately measure σ and A. This is achieved by recording images in the case of a homogeneous concentration of fluorescent species for which a well-defined exponential decay was found, leading to $\sigma = 1.27 \times 10^{-11}$ mm^2 and the multiplicative constant $A = 2.3 \times 10^{-5}$ (greylevel) part^{-1} ml for $t_e = 50$ ms. Note that A is not specific to the fluorescent species, but changes when the laser power, the exposure time or the optical set-up is modified. Finally, because the exponential decay is small here and can be considered as a first-order correction, the concentration field is finally obtained from (2.3) as

$$C(x,\, y,\, t) = \frac{I_{HDR}(x,\, y,\, t)}{A} \times \exp\left(\frac{\sigma}{A} \int_x^{L_{tot}} I_{HDR}(x',\, y,\, t)\, \mathrm{d}x'\right). \tag{2.4}$$

Using this procedure, the global mean concentration of the fluorescent species,

$$\langle C \rangle = \frac{1}{L_{tot} \times h} \int_0^{L_{tot}} \int_0^{h} C(x,\, y,\, t)\, \mathrm{d}x\, \mathrm{d}y = \frac{1}{L_{tot}} \int_0^{L_{tot}} C(x,\, t)\, \mathrm{d}x, \tag{2.5}$$

is checked to be a conserved quantity. The HDR profile of figure 3(*c*) is transformed into a concentration profile as plotted in figure 3(*d*), where we compare the raw profile without exponential correction and the corrected profile. The correction is cumulative from right to left, and is approximately 25 % close to the injection point. Although such a correction may appear to be significant, shining the laser from the opposite side (figure 1) reduces its impact to values smaller than 5 % on first and second moments of the concentration field,

$$\langle x^p \rangle = \frac{1}{L_{tot}} \int_0^{L_{tot}} x^p\, \frac{C(x,\, t)}{\langle C \rangle}\, \mathrm{d}x, \quad p = 1,\, 2, \tag{2.6}$$

which are the quantities that we will consider in the sequel.

In the following, we apply all the methods described above to follow species in the cellular flow, first without diffusiophoresis, then when diffusiophoresis comes into play.

3. Single scalar transport in the cellular flow

We first characterise the motion of a single species in the cellular flow. In practice, the LiCl salt chosen is not fluorescent, so as to avoid any problem when dealing with diffusiophoresis (which involves both colloids and salt). In order to evaluate the salt profile, we begin with fluorescein, a species that we have already used (Mauger *et al.* 2016)

https://doi.org/10.1017/jfm.2025.10813 Published online by Cambridge University Press

	D (m^2 s^{-1})	Pe at $\Delta T = 1.0\,^\circ$C	Pe at $\Delta T = 1.5\,^\circ$C
Fluorescein	0.42×10^{-9}	5.63×10^3	8.81×10^3
Salt (LiCl)	1.3×10^{-9}	1.84×10^3	2.88×10^3
Colloids	2.2×10^{-12}	2.26×10^6	3.53×10^6

Table 1. Diffusion coefficient for fluorescein, salt (LiCl) and colloids, and corresponding Péclet number of the flow $Pe = UL/D$ for two extreme temperature differences, $\Delta T = 1.0\,^\circ$C and $\Delta T = 1.5\,^\circ$C. Here, D is a generic diffusion coefficient, and D_f, D_s, D_c are the corresponding values for fluorescein, salt and colloids, respectively.

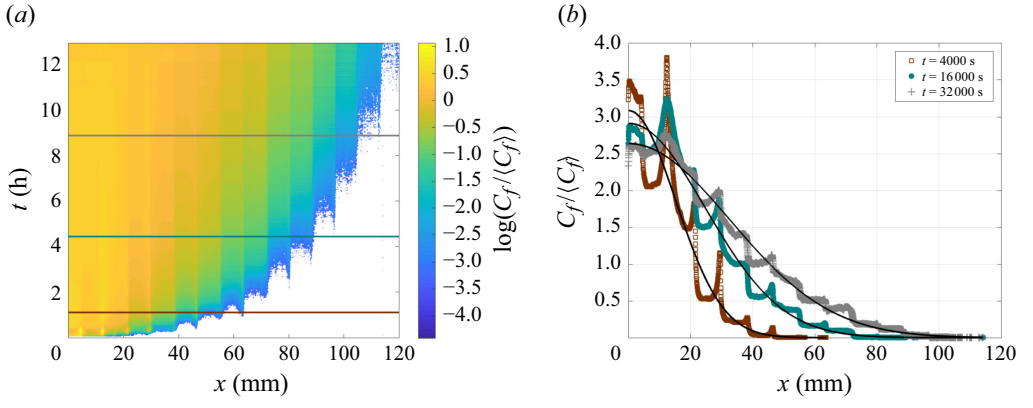


Figure 4. (*a*) Fluorescein concentration profile as a function of time for $\Delta T = 1.10 \pm 0.06\,^\circ$C ($Pe_f = 6270$). (*b*) Three concentration profiles extracted from (*a*) (corresponding to the three horizontal lines on this figure) for $t = 4000$ s (1 h 7 min), $t = 16\,000$ s (4 h 27 min) and $t = 32\,000$ s (8 h 53 min). Solid lines correspond to Gaussian functions with the same variance according to (3.1).

since its diffusion coefficient is very close to that of salt (see table 1), then we transpose to LiCl.

Quantities for fluorescein, salt and colloids are labelled with indices f, s and c, respectively. For example, we will denote the concentrations of fluorescein, salt and colloids as C_f, C_s and C_c, and their diffusion coefficients as D_f, D_s and D_c, with $Pe_f = UL/D_f$, $Pe_s = UL/D_s$ and $Pe_c = UL/D_c$ their corresponding Péclet numbers. Because the length L of the cells is fixed in all experiments, these Péclet numbers are directly proportional to velocity, hence they increase with the temperature difference ΔT between bottom and top. Therefore, for simplicity, a given experiment is characterised by ΔT afterwards. Relevant experimental parameters are summarised in table 1, where the diffusion coefficient of colloids is derived from the Stokes–Einstein equation, and the Péclet number $Pe = Uh/D$ based on the chamber height h is given for extreme temperature differences, $\Delta T = 1.0\,^\circ$C and $\Delta T = 1.5\,^\circ$C.

3.1. *Fluorescein profiles and effective diffusivities*

Fluorescein is introduced through injection site (1), and its concentration C_f is measured as a function of space and time. As seen in figure 4(*a*), which displays the time evolution of $\log(C_f(x,t)/\langle C_f\rangle)$, the one-dimensional concentration profiles are rather homogeneous in convection cells, with strong gradients in between. This is consistent with the observations of Solomon & Gollub (1988*b*), who reported that after several hours, the concentration

https://doi.org/10.1017/jfm.2025.10813 Published online by Cambridge University Press

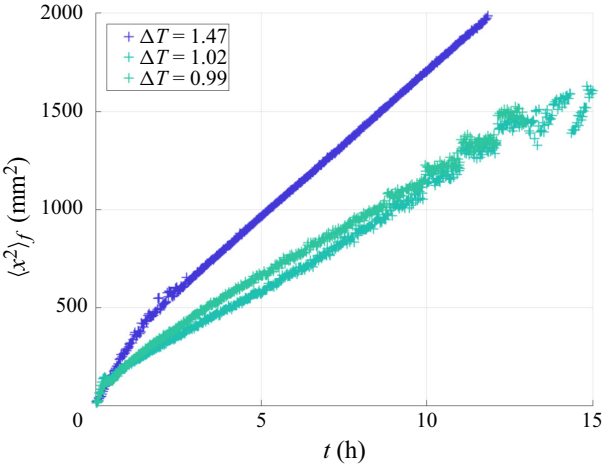


Figure 5. Typical dispersion curves for fluorescein and different values of the temperature difference $\Delta T = 0.99, 1.02, 1.47$ (corresponding to Péclet numbers of the fluorescein Pe_f between 5760 and 8630). As found previously in Solomon & Gollub (1988*b*), the global behaviour corresponds to an effective diffusion, with an effective diffusion coefficient given by (3.4).

becomes constant in each convection cell, the coarse-grained profile taking a Gaussian shape. This is also the case here, as shown in figure 4(*b*), where the scale evolution of the normalised profiles is well fitted by Gaussian functions with a maximum centred at the origin:

$$F(x,t) = \frac{N_{0,f}}{\sqrt{2\pi\ \langle x^2 \rangle_f(t)}} \exp\left(\frac{-x^2}{2\ \langle x^2 \rangle_f(t)}\right), \tag{3.1}$$

where $\langle x^2 \rangle_f(t)$ is the measured second-order moment for the fluorescein, computed following (2.6).

Solomon & Gollub (1988*b*) (see also Moffatt 1983; Pomeau 1985; Guyon *et al.* 1987; Shraiman 1987) proposed that such a Gaussian profile at large scale, where the concentration is homogenised through each cell, corresponds to a regime of effective diffusion in which the second-order moment of the distribution evolves linearly in time at large time

$$\langle x^2 \rangle(t) = \langle x^2 \rangle(0) + 2D^\star t \tag{3.2}$$

with an effective diffusion coefficient $D^\star$ such that

$$D^\star / D = B\ \sqrt{Pe}, \tag{3.3}$$

where B is a constant that depends on the geometry of the system, D is the diffusion coefficient, and Pe is the Péclet number.

Typical curves of the second-order moment $\langle x^2 \rangle_f(t)$ for the fluorescein and different Péclet numbers are shown in figure 5. After a rather long transient of approximately 2 hours, which corresponds to the time needed for invasion of a few cells, we observe that $\langle x^2 \rangle_f$ grows linearly in time, the slope being an increasing function of the Péclet number. Combining (3.2) and (3.3), and using a linear fit, we obtain

$$\langle x^2 \rangle_f(t) \approx \langle x^2 \rangle_f(0) + 2 \times B \times D_f\ \sqrt{Pe_f} \times t, \tag{3.4}$$

https://doi.org/10.1017/jfm.2025.10813 Published online by Cambridge University Press

with $\sqrt{\langle x^2\rangle_f(0)} \approx 12$ mm, which corresponds to a little more than one cell invaded by the fluorescein after injection at $t = 0$, and $B = 0.5$, which is consistent with what was found by Solomon & Gollub (1988*b*), given their definition of the Péclet number.

3.2. *Case of salt (LiCl)*

Salt (LiCl) is introduced at concentration 20 mmol l^{-1}, a concentration low enough so that no gravity current is created due to a possible density mismatch; it is then transported in the RB chamber in the same way as fluorescein. It is thus possible to estimate its dispersion from the results obtained for fluorescein, provided that its diffusion coefficient is slightly different, although of the same order of magnitude (see table 1). Therefore, we can extend the findings for flurorescein, and assume that the salt concentration also has a Gaussian coarse-grained profile over long time scales. We also differentiate between cases where salt is introduced through the injection holes (1) and (2). We thus obtain the following coarse-grained profile $S^{(i)}$ for the salt:

$$S^{(i)}(x,t) = \frac{N_{0,s}}{\sqrt{2\pi\ \langle x^2\rangle_s(t)}} \exp\left(\frac{-\left(L^{(i)}-x\right)^2}{2\,\langle x^2\rangle_s(t)}\right), \tag{3.5}$$

where $i = 1, 2$ stands for the injection hole through which the salt is injected, with $L^{(1)} = 0$ and $L^{(2)} = L_{tot}$. The variance $\langle x^2\rangle_s(t)$ of salt spreading does not depend on the salt's direction of travel, and is therefore identical in the two cases:

$$\langle x^2\rangle_s(t) \approx \langle x^2\rangle_s(0) + 2 \times B \times D_s\sqrt{Pe_s} \times t, \tag{3.6}$$

with $\sqrt{\langle x^2\rangle_s(0)} \approx 12$ mm and $B = 0.5$, as for fluorescein in (3.4).

3.3. *Colloids: reference case*

We now investigate how colloids are transported through the chamber in the reference case, i.e. without salt. Colloids are injected through site (1) at $t = 0$. From the images, we build one-dimensional normalised concentration profiles $C_c(x,t)/\langle C_c(x,t)\rangle$ averaged over the height of the chamber. Their typical time evolution is shown in figure 6(*a*) for $\Delta T = 1.1$ °C ($Pe_c = 3.9 \times 10^5$). As is clearly visible, the concentration field is much less homogeneized than in the case of fluorescein, with spatial oscillations and peaks located in between the cells even at long times. This is clearly visible when plotting directly the normalised concentration $C_c/\langle C_c\rangle$ at different times, as displayed in figure 6(*b*). Such a difference between profiles measured in the case of particles and molecules in the chamber was already pointed out by Solomon & Gollub (1988*b*), who mentioned that homogenisation does not really take place in the cells in the case of latex particles, due to their large size and hence weak diffusion coefficient. A first noticeable difference with results from Solomon & Gollub (1988*b*) is that the colloid concentration profiles can hardly be described as Gaussian functions, even more than 16 hours after injection. Another difference can be seen in figure 6(*c*), which displays the time evolution of the second-order moment of the colloid concentration field, $\langle x^2\rangle_c$, for seven different Péclet numbers $Pe_c \in [1.1, 1.5] \times 10^6$. In none of the different runs was it possible to observe a well-defined linear evolution for the colloid concentration field, even after repeating the same experiment several times. An explanation for this could be the presence of an additional three-dimensional structure to the flow that would modify mixing, making the concentration field more complex than with two-dimensional flow. However, the contribution of such a three-dimensional structure was already mentioned in Solomon & Gollub (1988*b*), and was also present in the case of fluorescein, for which we obtained

https://doi.org/10.1017/jfm.2025.10813 Published online by Cambridge University Press

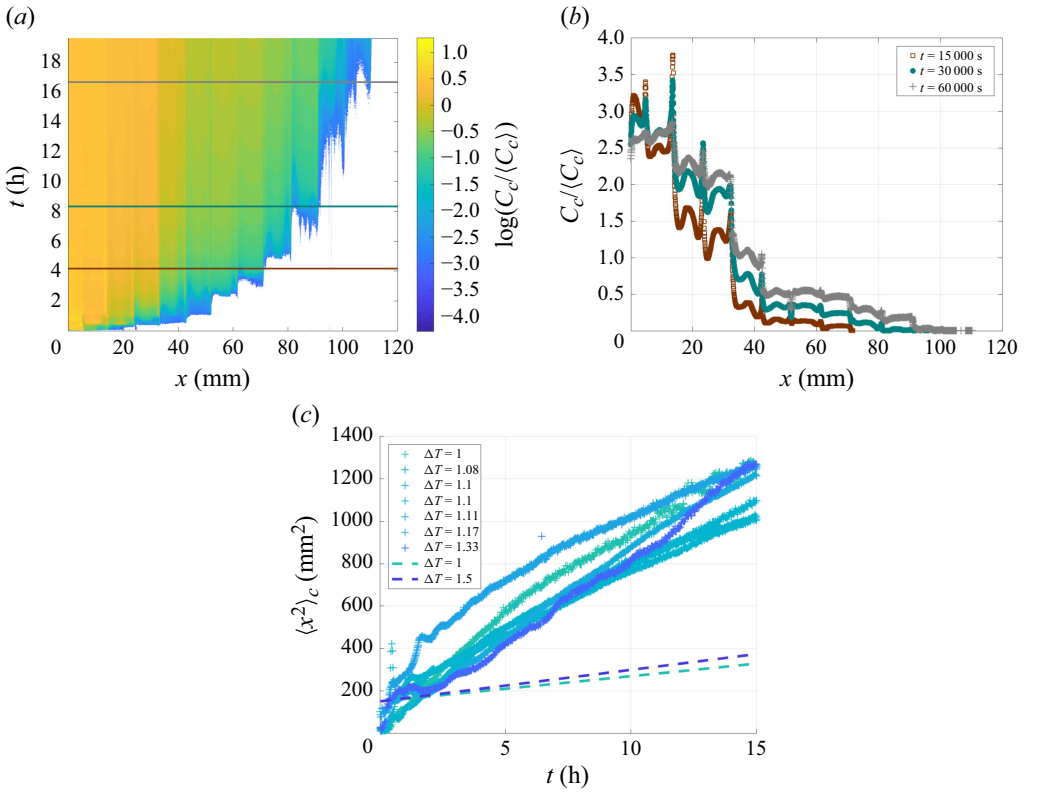


Figure 6. Reference case (colloids alone). (*a*) Normalised colloid concentration profile as a function of time for $\Delta T = 1.1$ °C ($Pe_c = 3.9 \times 10^5$). (*b*) Three concentration profiles extracted from (*a*) (corresponding to the three horizontal lines on this figure) for $t = 15\,000$ s (4 h 10 min), $t = 30\,000$ s (8 h 20 min) and $t = 60\,000$ s (16 h 40 min). (*c*) Dispersion curves $\langle x^2\rangle_c(t)$ obtained with colloids and temperature difference $\Delta T \in [1, 1.33]$ °C. The darker the symbol, the larger the colloid Péclet number. The two dashed lines stand for the theoretical predictions for the spreading of neutral particles of the same size as the colloids, calculated using (3.4) transposed to colloids, $\langle x^2\rangle_c(t) \approx \langle x^2\rangle_c(0) + 2 \times B \times D_c\sqrt{Pe_c} \times t$, with $\sqrt{\langle x^2\rangle_c(0)} \approx 12$ mm and $B = 0.5$ as for fluorescein (3.4), for $\Delta T = 1$ °C and $\Delta T = 1.5$ °C.

$\langle x^2\rangle_f \propto t$ at long times. This means that we need to look for another mechanism that is present in the case of (charged) colloidal particles but not in solutes.

Indeed, another major difference with the work by Solomon & Gollub (1988*b*) is that the effective diffusion coefficient estimated for the different values of ΔT (hence Pe_c) is much larger than expected, as can be seen from figure 6(*c*), in which the dashed lines represent the theoretical prediction (3.4) transposed to neutral particles of the same size. At these small concentration levels, this cannot be related to a collective effect of colloids. Another possibility is the existence of thermophoretic effects, whereby large particles exhibit a drift velocity related to thermal gradients. However, this would imply that the effect increases with rising ΔT, which is not the case here, as can be seen in figure 6(*c*), where the effective diffusion is almost independent of ΔT. One can also note that the top–bottom symmetry of the observed pattern in figure 7, which displays the snapshot of a typical reference case, definitely contradicts the thermophoresis hypothesis. More likely, the explanation may come from the fact that because we need to study diffusiophoretic effects, our particles are (positively) charged, and hence may interact with the upper and lower walls made of brass, which takes a negative charge in water (Sarver *et al.* 2016; Cui *et al.* 2024).

https://doi.org/10.1017/jfm.2025.10813 Published online by Cambridge University Press

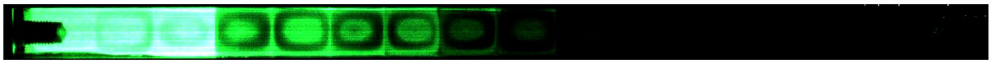


Figure 7. Typical image of a reference case ($\Delta T = 1.1$ °C and $t = 43\,000$ s $= 12$ h).

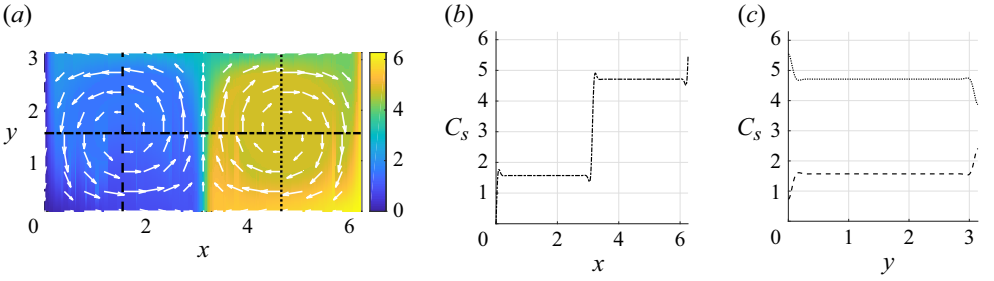


Figure 8. Salt distribution (numerical simulations) in the stationary regime, for a constant horizontal mean gradient $\boldsymbol{G} = G\,\boldsymbol{e}_x$; here, $Pe_s = 3140$, $G = 1$, and the size of a cell is $L = \pi$. (a) Stationary salt concentration field C_s in two consecutive cells, with an imposed constant mean gradient $\boldsymbol{G} = G\,\boldsymbol{e}_x$; the white arrows represent the cellular velocity field. (b) Horizontal profile along the horizontal dashed line in (a). (c) Two vertical profiles along the vertical dashed lines. The salt concentration is approximately constant in the cells, except around the vertical and horizontal separatrixes.

This additional mechanism tends to facilitate the diffusion of particles along the separatrixes of the flow, leading to a much larger dispersion. This hypothesis is reinforced when looking at figure 7, where we clearly see that colloids are attracted to the walls; this effect was not present in Solomon & Gollub (1988*b*).

4. Diffusiophoresis and cellular flow

In this section, we first summarise the theoretical results obtained in Volk *et al.* (2022), in order to transpose them to the experiment afterwards. In particular, we want to check whether our experimental conditions could lead to the regime of enhanced transport, or else to blockage.

4.1. *Theory from Volk et al. (2022)*

The theoretical results in Volk *et al.* (2022) were obtained in stationary conditions. The advection–diffusion equation was first solved numerically for the salt concentration C_s in the presence of an imposed mean salt gradient $\boldsymbol{G}$, using an analytical cellular velocity field $\boldsymbol{u}$. In the stationary regime, this results in a solution where the salt concentration is almost constant within each cell, except in the vicinity of the separatrixes; see figure 8(a) for an example with $Pe_s = 1340$. The horizontal profile shown in figure 8(b) exhibits a sharp increase of magnitude $\Delta S = G \times L$ between two consecutive cells, indicating a very high salt gradient. The width ℓ_s of this gradient is found by the competition between contraction by the flow (typical time L/U) and diffusion (typical time ℓ_s^2/D_s), hence $\ell_s \sim L/\sqrt{Pe_s}$, and the corresponding salt gradient in this region is $\Delta S/\ell_s \sim G\sqrt{Pe_s} \gg G$. Note that the vertical profiles in figure 8(c) also show a small vertical salt gradient around the horizontal separatrixes, but of much weaker intensity; hence we neglect it in a first step.

We now consider the displacement of colloids in this salt distribution. In Volk *et al.* (2022), the drift velocity of the active particles is of the type $\boldsymbol{v}_{dp} = \alpha\,\boldsymbol{\nabla} C_s$, where α is the phoretic coefficient. The total velocity of a phoretic particle is thus $\boldsymbol{v} = \boldsymbol{u} + \boldsymbol{v}_{dp}$, where $v_{dp} \ll U$. When a particle enters the salt gradient (shown in light blue in

https://doi.org/10.1017/jfm.2025.10813 Published online by Cambridge University Press

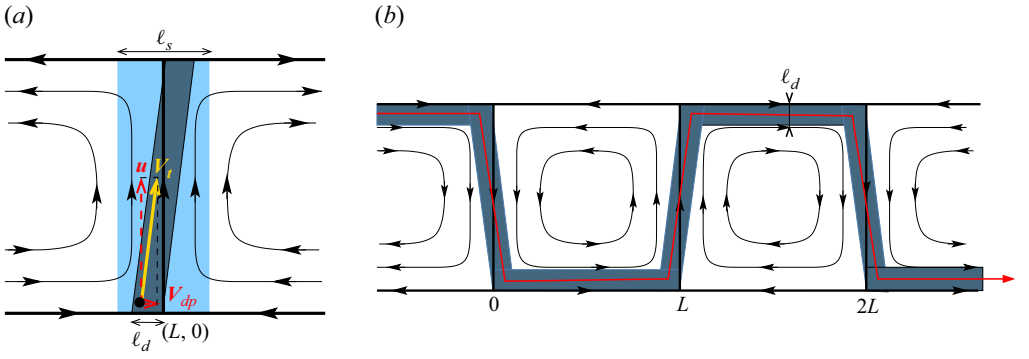


Figure 9. (*a*) Schematic displacement of a particle in the salt gradient (light blue region) around the vertical ascending separatrix $x = L$. The Eulerian velocity field $\boldsymbol{u}$ is vertical and ascending, and $\boldsymbol{v}_{dp}$ is horizontal; the total velocity of particles around the vertical separatrixes is therefore $\boldsymbol{v}_t = \boldsymbol{u} + \boldsymbol{v}_{dp}$, with $\boldsymbol{u} \approx U\,\boldsymbol{e}_y$. Particles that change cell are located on the grey strip of width ℓ_d. (*b*) Schematic location of particles that change cell, in grey, for cells located between $x = 0$ and $x = 2L$; an example of a trajectory is shown in red. Outside this grey strip, the particles remain trapped in their cells. From Volk *et al.* (2022).

figure 9(*a*)), it deviates horizontally by a distance ℓ_d such that $\ell_d/L = v_{dp}/U$, so that $\ell_d \sim \alpha G L\sqrt{Pe_s}/U$. The particles that change cell are located within the grey strip of width ℓ_d in figure 9(*a*). These particles are then transported horizontally by the velocity field until they reach the next region of high salt gradient, thus travelling around the cells, globally in the direction of the mean salt gradient $\boldsymbol{G}$, as depicted in figure 9(*b*). As the particles located outside the grey strip do not change cell, it is possible to estimate the mean global horizontal velocity as $v_m \sim 1/L^2 \times [(\ell_d \times L)\, v_{dp} + (\ell_d \times L)\, U]$. Finally, because $v_{dp} \ll U$, we obtain

$$v_m \sim \alpha G\sqrt{Pe_s}. \tag{4.1}$$

This regime, for which the mean velocity is much higher than the velocity, αG, associated with the mean salt gradient, is called 'enhanced transport'. Lagrangian numerical simulations performed in Volk *et al.* (2022) show that (4.1) gives a good estimation of the global mean velocity.

The blockage regime is related to the weaker vertical salt gradients around the horizontal separatrixes; see figure 8(*c*). Indeed, because the salt concentration increases from left to right due to the imposed mean gradient $\boldsymbol{G}$, the velocity field transports a deficit of salt when travelling horizontally from left to right, and an excess of salt when travelling in the opposite direction, as is visible in figure 8(*a*). Therefore, the phoretic particles located within a horizontal segment of the grey strip in figure 9(*b*) always encounter a salt gradient pointing vertically into the cell, and gradually deviate towards its centre: after some time, they leave the grey strip for the central region of the cell. Once all the particles have left the strip, they can no longer change cell, and become blocked. In addition, any fluid particle located inside the strip follows the velocity field and completes one revolution around the cell in a typical time $4L/U$. This creates a corona of width ℓ_d devoid of particles around each cell, as demonstrated numerically in Volk *et al.* (2022) (see also figure 16 below for an experimental visualisation).

This blocking mechanism occurs only when diffusion is insufficient to bring particles back into the strip. Therefore, we need to estimate how long it takes for particles outside the strip to re-enter it. Consider a strip of width ℓ_d that is empty of particles in a medium that is filled with particles. Due to the linearity of the advection–diffusion equation, the

https://doi.org/10.1017/jfm.2025.10813 Published online by Cambridge University Press

problem is the same as considering a strip of width ℓ_d filled with particles in an empty medium: the typical diffusion time is, in both cases, ℓ_d^2/D_c.

Blockage therefore corresponds to a situation in which fluid in the empty corona can travel around the cell while remaining empty of particles, i.e. $4L/U \ll \ell_d^2/D_c$. Introducing the blockage parameter R such that

$$R = \frac{\alpha\, GL}{2\sqrt{D_c D_s}}, \tag{4.2}$$

we obtain the blockage situation corresponding to $R \gg 1$.

Numerical simulations performed in Volk *et al.* (2022) demonstrate a sharp transition between blockage and enhanced transport, depending on R: a complete blockage is observed whenever $R \geqslant 4$, while enhanced transport, with a magnitude given by (4.1), corresponds to $R \leqslant 1$; in practice, enhanced transport is already observed for $R \sim 2$, although with a weaker velocity. This is all explained in much more detail in Volk *et al.* (2022).

4.2. *Experiment versus theory*

Although there are some differences between the experiment and the theory, we now demonstrate how the theoretical findings can be adapted to the experimental conditions.

4.2.1. *Velocity field*

In the theory, numerical work and experiments, the velocity field is steady and cellular. There are some minor discrepancies, such as the boundary conditions applied to the upper and lower walls (no-slip in the experiment, and slip in the numerical analysis), but it should be noted that the theory is not heavily dependent on the specifics of the flow. On the one hand, the enhanced transport regime only depends on the salt Péclet number Pe_s, based on the maximum velocity U, as shown in (4.1). On the other hand, the blockage parameter R in (4.2) does not depend on the velocity at all. Therefore, we can conclude that the theory and the experiment are very similar in this respect.

Finally, the major difference between the theory and the experiment is that the former considers an infinite medium, whereas the latter has a finite extent. This is not important when considering the blockage situation, but it will be important when considering enhanced dispersion.

4.2.2. *Salt distribution*

The situation regarding the distribution of salt is very different: the theory assumes an imposed mean salt gradient, which is assumed to be constant in space and time. Furthermore, the theory deals with the stationary solution of the advection–diffusion equation. By contrast, the salt distribution in the experiment is time-dependent and follows a Gaussian coarse-grained profile, denoted by S (see (3.5)). The experimental equivalent for G is the horizontal salt concentration jump across a cell, divided by the cell's length L. This jump in salt concentration can be estimated rather accurately using the coarse-grained profile S. If we denote as $G^{(i)}$ the mean horizontal salt gradient across a cell in the case when salt is introduced through site (i), then $G^{(i)} \approx \mathrm{d}S/\mathrm{d}x$, so that we obtain from (3.5) that

$$G^{(i)}(x,t) = \frac{x - L^{(i)}}{\langle x^2\rangle_s(t)} \times S(x,t), \tag{4.3}$$

where we recall that $L^{(1)} = 0$ and $L^{(2)} = L_{tot}$.

https://doi.org/10.1017/jfm.2025.10813 Published online by Cambridge University Press

4.2.3. *Velocity drift*

As stated in § 4.1, in Volk *et al.* (2022), the drift velocity due to phoresis was taken as $\boldsymbol{v}_{dp} = \alpha\, \boldsymbol{\nabla} C_s$. However, the relationship between drift velocity and scalar gradients is generally much more complex (Gupta, Shim & Stone 2020; Lee, Lee & Ault 2023). For very charged particles such as ours, the drift velocity takes the form (Ault & Shi 2025)

$$\boldsymbol{v}_{dp} = D_{dp}\, \boldsymbol{\nabla} \log C_s = D_{dp} \frac{\boldsymbol{\nabla} C_s}{C_s}. \tag{4.4}$$

Then we switch from theory to experiment by setting $\alpha \approx D_{dp}/C_s$, or rather $\alpha \approx D_{dp}/S$ when dealing with mean quantities as in (4.1) or (4.2). Note also that the experiments may be non-repeatable in the case of salt concentrations C_s that are too small, far from the injection hole at early times. This will be taken into account later.

4.2.4. *Enhanced transport*

Even if the theoretical formulas (4.1) and (4.2) were derived in a stationary regime, they may still apply to a transient case, provided that the salt evolves slowly over time, as is the case in the experiment. From the analysis above, we can transpose the value found for enhanced transport in (4.1) to the experimental conditions. We obtain

$$v_m^{(i)}(x, t) \sim D_{dp}\sqrt{Pe_s}\, \frac{L^{(i)} - x}{\langle x^2 \rangle_s(t)}, \tag{4.5}$$

where again $i = 1, 2$ stands for the injection site. We observe that the velocity due to salt attraction is also inhomogeneous and time-dependent. When $i = 1$ ($L^{(1)} = 0$), the velocity is negative, as expected for colloids that move in the direction of the salt gradient; conversely, when $i = 2$ ($L^{(2)} = L_{tot}$), the velocity is positive. Note also that the effect decays over time, but increases with the Péclet number.

4.2.5. *Blockage coefficient*

We now transpose the theoretical blockage coefficient (4.2) to experimental conditions. Unlike enhanced transport, blockage does not depend on the direction of the salt gradient. Therefore, the blockage coefficient is always positive and is given by

$$R^{(i)}(x, t) = \frac{|L^{(i)} - x| \times L}{2\, \langle x^2 \rangle_s(t)} \times \frac{D_{dp}}{\sqrt{D_c D_s}}. \tag{4.6}$$

In the experiment, we have $D_s = 1360\,\mu\mathrm{m}^2\,\mathrm{s}^{-1}$, $D_c = 2\,\mu\mathrm{m}^2\,\mathrm{s}^{-1}$ and $D_{dp} = 290\,\mu\mathrm{m}^2\,\mathrm{s}^{-1}$, so that $D_{dp}/\sqrt{D_c D_s} \approx 5.56$. Because the theory predicts blockage for $R \geqslant 4$, it may be possible to observe blockage at some location. Note also that $\langle x^2 \rangle_s(t)$ increases with time, implying that the blockage coefficient R decreases with time at a given point x, so that blockage is not possible at long time.

However, the value of the blockage coefficient cannot be transposed directly to the experiment status. Indeed, the theory was derived in the context of an infinite and periodic medium, and in a stationary state: the conditions in the experiment differ greatly from these.

The differences between theory and experiment are summarised in table 2. In the following, we explain the consequences for both the enhanced transport and blockage configurations.

https://doi.org/10.1017/jfm.2025.10813 Published online by Cambridge University Press

	Theory	Experiment
Velocity field	Cellullar and steady Infinite medium	Cellullar and steady Finite extent
Salt distribution	Stationary	Non-stationary
	Imposed constant mean gradient G	Mean gradient $G^{(i)}(x,t) = \dfrac{x - L^{(i)}}{\langle x^2 \rangle_s(t)} \times S(x,t)$
Drift velocity	$\boldsymbol{v}_{dp} = \alpha\, \boldsymbol{\nabla} C_s$	$\boldsymbol{v}_{dp} = D_{dp}\, \boldsymbol{\nabla} \log C_s = D_{dp} \dfrac{\boldsymbol{\nabla} C_s}{C_s}$
Enhanced transport	$v_m \sim \alpha G \sqrt{Pe_s}$	$v_m^{(i)}(x,t) \sim D_{dp} \sqrt{Pe_s}\, \dfrac{L^{(i)} - x}{\langle x^2 \rangle_s(t)}$
Blockage coefficient	$R = \dfrac{\alpha\, G L}{2\sqrt{D_c D_s}}$	$R^{(i)}(x,t) = \dfrac{\lvert L^{(i)} - x \rvert \times L}{2\, \langle x^2 \rangle_s(t)} \times \dfrac{D_{dp}}{\sqrt{D_c D_s}}$

Table 2. Summary of the differences between theory and experimental conditions. For the experiment, the index $i = 1, 2$ stands for the injection hole of the salt (see figure 1), with $L^{(1)} = 0$ and $L^{(2)} = L_{tot}$.

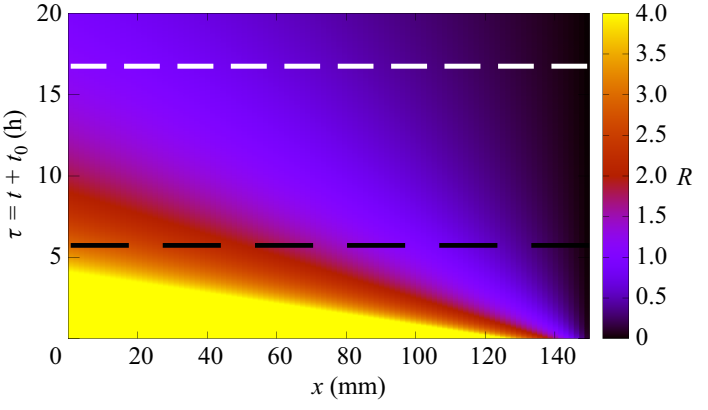


Figure 10. Space-time diagram for the blockage coefficient R in the salt-out configuration (4.7) for $\Delta T = 1\,^{\circ}\mathrm{C}$, with the experimental data $D_s = 1360\ \mu\mathrm{m}^2\ \mathrm{s}^{-1}$, $D_c = 2\ \mu\mathrm{m}^2\ \mathrm{s}^{-1}$ and $D_{dp} = 290\ \mu\mathrm{m}^2\ \mathrm{s}^{-1}$ ($D_{dp}/\sqrt{D_c D_s} \approx 5.56$). Values higher than 4, which correspond to possible blockage, are shown in yellow. The salt is released at time $\tau = 0$, while the colloids are released a time t_0 later; we set $t = \tau - t_0$ so as to have the colloids released at $t = 0$. The dashed lines indicate the times at which the colloids are released in the experiments presented: black dashed line for $t_0 = 6$ h; white dashed line for $t_0 = 17$ h.

4.3. *Salt-out configuration: enhanced transport*

In practice, blockage or enhanced transport could, in theory, be observed regardless of the configuration considered (salt-in or salt-out). Indeed, let us come back to the value of the blockage coefficient. In the salt-out configuration, it is obtained by letting $i = 2$ in (4.6):

$$R^{salt\text{-}out}(x,t) = \frac{(L_{tot} - x) \times L}{2\, \langle x^2 \rangle_s(t)} \times \frac{D_{dp}}{\sqrt{D_c D_s}}. \tag{4.7}$$

The space–time diagram for $R^{salt\text{-}out}$ is shown in figure 10; values higher than 4, corresponding to possible blockage, are coloured yellow. The diagram shows high values of R (in yellow) at short times in the region where the colloids are injected and initially

https://doi.org/10.1017/jfm.2025.10813 Published online by Cambridge University Press

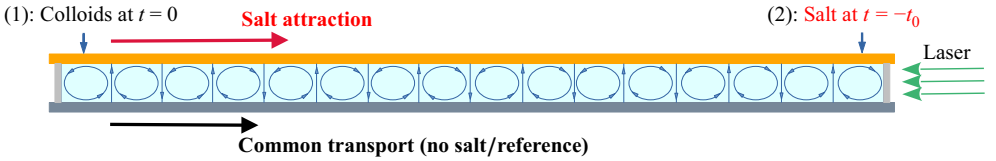


Figure 11. Salt-out configuration: first, salt (LiCl, non-fluorescent) is introduced through injection site (2) at $t = -t_0$; then colloids (fluorescent) are introduced through injection site (1) at $t = 0$. The delay t_0 must be long enough so that some salt has reached the other side of the cell when colloids are introduced. The two horizontal bold arrows show the transient effects felt by the colloids after introduction: they naturally travel towards the right, as showed in the reference case (common transport); they are also attracted by salt and therefore furthermore travel towards the right (salt attraction).

spread, which is consistent with possible blockage. However, blockage is not physically reasonable: actually, as previously explained, the salt Gaussian coarse-grained profile used in the calculation does not settle instantaneously in the chamber. Furthermore, it takes time for the salt to travel across the whole cell towards the colloids. Finally, note that these large values of R would correspond to very small salt concentrations here, which could lead to non-repeatable experiments (see (4.4)). Therefore, the salt must be injected into the cell well before the colloids, so as to have reached the injection site (1) when the colloids are introduced; as shown in figure 11, salt is introduced at time $t = -t_0$, with $t_0 > 0$ the time lag before the colloids injection. We let $\tau = t + t_0$; salt is therefore introduced at $\tau = 0$ in this time coordinate, and $\langle x^2\rangle_s(\tau)$ verifies (3.6) exactly. We can write

$$\langle x^2\rangle_s(\tau) = \langle x^2\rangle_s(t + t_0) \approx \langle x^2\rangle_s(0) + 2 \times B \times D_s\sqrt{Pe_s} \times (t + t_0), \tag{4.8}$$

with $\sqrt{\langle x^2\rangle_s(0)} \approx 12$ mm and $B \approx 0.5$ from (3.6).

In practice, we found no noticeable diffusiophoretic effect of salt on the colloids whenever the time lag t_0 was shorter than 5–6 hours. In figure 10, the line corresponding to the time lag $t_0 = 6$ h, corresponding to one of our experiments, is plotted as a black dashed line; as can be seen, at that time, the blockage coefficient R is already too small to have blockage. Furthermore, all transient effects (i.e. the common transport of colloids and salt attraction) tend to move the colloids to the right (figure 11), which works against blockage. Finally, note that R decreases from left to right, in the direction of colloid movement. Therefore, the salt-out configuration is highly unlikely to exhibit blockage, but it may result in enhanced transport.

We now apply (4.5) with $i = 2$ ($L^{(2)} = L_{tot}$) and obtain

$$v_m(x, t) \sim D_{dp}\sqrt{Pe_s}\,\frac{L_{tot} - x}{\langle x^2\rangle_s(t + t_0)}, \tag{4.9}$$

with $\langle x^2\rangle_s$ given by (4.8). This equation can be averaged over the colloid concentration profile to obtain the global mean velocity of colloids in the chamber $V_m(t) = \langle v_m(x, t)\rangle_c$:

$$V_m(t) = \frac{1}{L_{tot}\,\langle C\rangle}\int_0^{L_{tot}} C(x)\, v_m(x)\,\mathrm{d}x \sim \frac{D_{dp}\sqrt{Pe_s}}{\langle x^2\rangle_s(t + t_0)}\left(L_{tot} - \langle x\rangle_c(t)\right). \tag{4.10}$$

Using the equality

$$V_m(t) = \frac{\mathrm{d}\langle x\rangle_c(t)}{\mathrm{d}t}, \tag{4.11}$$

https://doi.org/10.1017/jfm.2025.10813 Published online by Cambridge University Press

it is possible to predict the evolution of $\langle x\rangle_c(t)$. Indeed, combining (4.10) and (4.11), we obtain

$$\frac{\mathrm{d}\langle x\rangle_c}{L_{tot}-\langle x\rangle_c(t)} = D_{dp}\sqrt{Pe_s}\,\frac{\mathrm{d}t}{\langle x^2\rangle_s(t+t_0)}, \tag{4.12}$$

with $\langle x^2\rangle_s(t+t_0) = a + b(t_0+t)$ from (4.8). This can therefore be integrated into

$$-\ln\frac{L_{tot}-\langle x\rangle_c(t)}{L_{tot}-\langle x\rangle_c(0)} = D_{dp}\sqrt{Pe_s}\times\frac{1}{b}\,\ln\frac{a+b(t_0+t)}{a+b\,t_0}. \tag{4.13}$$

Introducing the non-dimensional coefficient

$$\beta = D_{dp}\sqrt{Pe_s}\times\frac{1}{b} = \frac{D_{dp}\sqrt{Pe_s}}{2D_s^\star}, \tag{4.14}$$

which verifies $\beta\sim(D_{dp}/D_s)<1$ as $D_s^\star\sim 0.5\,D_s\sqrt{Pe_s}$, we finally obtain

$$\begin{aligned}\langle x\rangle_c(t) &= L_{tot}-\big(L_{tot}-\langle x\rangle_c(0)\big)\left(\frac{a+b\,t_0}{a+b\,(t_0+t)}\right)^{\beta}\\ &= L_{tot}-\big(L_{tot}-\langle x\rangle_c(0)\big)\left(\frac{\langle x^2\rangle_s(t_0)}{\langle x^2\rangle_s(t_0+t)}\right)^{\beta},\end{aligned} \tag{4.15}$$

with a and b given in (3.6), and β given by (4.14).

The formula implies that as $t\to\infty$, the ratio of salt dispersion becomes small, and $\langle x\rangle_c(t)$ tends to L_{tot}; physically, one would rather think of $L_{tot}/2$. But of course there is no diffusion in those calculations, only physics of particles that move with a velocity proportional to ∇S, which only cancels at $x=L_{tot}$. Similarly, at short time we have

$$\langle x\rangle_c(t)\underset{t\to 0}{\sim} L_{tot}-\big(L_{tot}-\langle x\rangle_c(0)\big)\times\left(1-\frac{D_{dp}\sqrt{Pe_s}}{\langle x^2\rangle_s(t_0)}t\right), \tag{4.16}$$

so that the slope at the origin is all the more important as t_0 is small. As previously explained, this is, of course, not valid if colloids are introduced too early after salt injection ($t_0\leqslant 5$ h), since the calculation assumes that the salt Gaussian profile has been established throughout the cell.

The experimental results in the salt-out configuration are shown in figure 12, for two different values of the time lag t_0, and rather similar Péclet numbers ($\Delta T = 1.03\,^\circ$C and $1.1\,^\circ$C). On the right, the magenta curves show the mean longitudinal profile $\langle x\rangle_c(t)$; for comparison, the black curves show the same quantity in a reference case (colloids with no salt). First, one can notice that the effect of salt compared to the reference, although visible, is not as important as supposed from the theory. Indeed, as explained before, due to their charge, the colloids spread much more rapidly in the cell than what is expected for non-charged particles (see also figure 6*c*). The theoretical prediction for the salt effect (4.16) is plotted as a dash-dotted blue line for the two time lags. As can be seen, the order of magnitude of the salt effect is rather well predicted by (4.16). Indeed, as shown in figure 10, these two time lags correspond to moments when the blockage coefficient is far enough from blockage conditions so as to allow enhanced transport. This is completely achieved for $t_0 = 17$ h (white dashed line), but also true for $t_0 = 6$ h (black dashed line) provided that $x\geqslant 10$ mm, i.e. from the second cell onwards.

After some time, the experimental profile no longer keeps up with the prediction, but rather follows the same slope (hence same velocity) as the reference. This can be explained easily from the fact that the experiment has a finite size: indeed, in the theory, the regime

https://doi.org/10.1017/jfm.2025.10813 Published online by Cambridge University Press

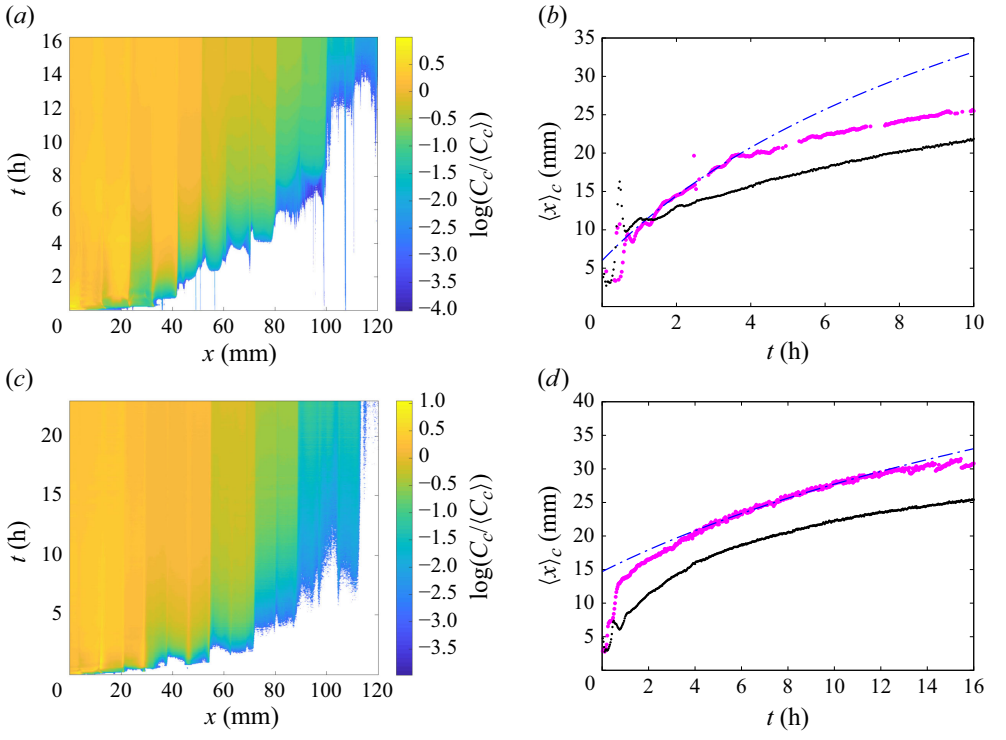


Figure 12. Salt-out case. (*a*,*c*) Colloid concentration profile as a function of time for two different time lags t_0. (*b*,*d*) Corresponding $\langle x\rangle_c$ as a function of time (magenta curve). The dash-dotted blue line is the theoretical prediction (4.16). For comparison, the black curve is a reference case (colloids with no salt) for a similar Péclet number. Here, (*a*,*b*) $t_0 = 6$ h ($\Delta T = 1.03$ °C) and (*c*,*d*) $t_0 = 17$ h ($\Delta T = 1.1$ °C).

of enhanced transport derives from a strip of colloids that travels in the direction of the mean salt gradient from left to right; see figure 9. In the theory, the domain is infinite, so there are always colloids arriving from the left. Because the experiment is finite, after a while, the strip on the left has emptied and cannot be renewed, which stops the process. We can estimate the time spent by the colloids in the strip to cross the whole cell. The time needed to change cell is $\ell_d/v_{dp} \sim L/U$; see figure 9(*a*). Since there are N cells in the chamber, the total time spent by particles to cross all the vertical gradients is $(N-1)\times L/U \approx L_{tot}/U$. Outside the salt gradient, the colloids are transported by the flow; see figure 9(*b*). Therefore the time spent by a colloid to cross a cell from one vertical salt gradient to the other is also L/U, with a total time in the horizontal strips of the order of L_{tot}/U. Finally, the total time spent by the colloids initially in the left strip to cross the entire cell is $\tau_{cell} \sim 2\times L_{tot}/U$. With a maximum velocity $U \sim 0.3$ mm s^{-1}, we obtain for our experiment $\tau_{cell} \sim 15$ min. This result must be taken with caution: of course, the velocity near the top and bottom walls may be smaller than the maximum velocity U. But, more problematically, the velocity v_{dp} in the salt gradient is very small; therefore a small error/change in v_{dp} may lead to a quite different result. For instance, in figure 12(*b*) ($t_0 = 6$ h), we observe that, once settled, the experimental profile follows the theory of enhanced transport during 2–3 hours, before following the same slope as the reference (common transport). Although this lapse of time is rather higher than what is predicted by the theory, its order of magnitude is still reasonable, which validates the hypothesis. In the case $t_0 = 17$ h (figure 12*d*), there is no clear transition as in the preceding case, since the slope predicted by the theory is only slighly higher than what is observed without salt.

https://doi.org/10.1017/jfm.2025.10813 Published online by Cambridge University Press

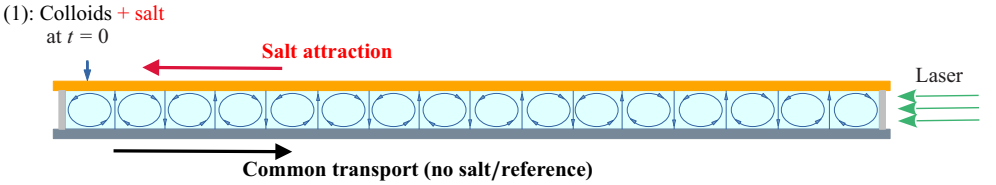


Figure 13. Salt-in configuration: fluorescent colloids, together with non-fluorescent LiCl salt, are introduced through injection site (1) at $t = 0$. The two horizontal bold arrows show the transient effects felt by the colloids after introduction: they naturally tend to travel towards the right, as shown in the reference case (common transport); they are also attracted by salt and therefore also tend to travel towards the left. There is thus a competition at small time between the two processes.

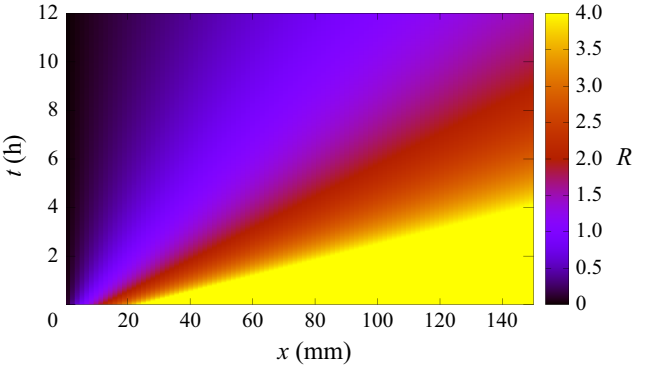


Figure 14. Space–time diagram for the blockage coefficient R in the salt-in configuration for $\Delta T = 1\,^{\circ}\mathrm{C}$. Values higher than 4, which correspond to possible blockage, are shown in yellow. Both salt and colloids are released at time $t = 0$ (see figure 13).

4.4. *Salt-in configuration: blockage*

We now turn to the salt-in configuration, depicted in figure 13: fluorescent colloids are introduced together with non-fluorescent LiCl salt at $t = 0$ through injection site (1). As before, we track the fluorescent species so as to measure the local concentration at each point.

Because salt travels more rapidly than the colloidal particles, one can assume that the Gaussian salt profile seen by the colloids is rapidly settled from the injection point (1). In this case, the blockage coefficient reads, from (4.6) with $i = 1$ and $L^{(1)} = 0$,

$$R^{salt\text{-}in}(x, t) = \frac{x \times L}{2\,\langle x^2\rangle_s(t)} \times \frac{D_{dp}}{\sqrt{D_c D_s}}, \tag{4.17}$$

with $\langle x^2\rangle_s(t)$ given by (3.6). Figure 14 displays the space diagram for the blockage coefficient in the salt-in configuration, for $\Delta T = 1\,^{\circ}\mathrm{C}$. It shows that blockage is possible over a short period of time once the colloids have travelled far enough away from the injection site (1); in practice, a few cells is enough. However, this coefficient was derived under stationary conditions. In practice, blockage does not occur instantly, and the transient effects that take place in the cell before blockage may happen must be taken into account. The first of these, as seen in figure 13, is again the common transport that takes place even without salt and tends to move the colloids to the right. Although one could then think that it should help blockage (the blockage coefficient is larger further from the injection site), in fact it prevents blockage since colloids that change cell are those located

https://doi.org/10.1017/jfm.2025.10813 Published online by Cambridge University Press

near the walls (figure 7). Colloids that get blocked must have remained long enough in their cell, far from the wall. The second transient effect is still related to salt attraction, and in those conditions makes colloids located near the walls (figure 9) travel to the left. Therefore, the two effects push in opposite directions, so blockage is more likely to be observed. The condition $R \geqslant 4$ implies, from (4.17),

$$\frac{x}{L} \geqslant 8\,\frac{\langle x^2\rangle_s(t)}{L^2}\,\frac{\sqrt{D_c D_s}}{D_{dp}}, \tag{4.18}$$

where (4.18) is therefore a necessary condition of blockage.

The concentration profiles in x are shown in figure 15(a,c,e), together with their corresponding mean profiles $\langle x\rangle_c(t)$ in figure 15(b,d,f), for three different values of the temperature difference ΔT (hence different Péclet numbers). In figure 15(a,c,e), the solid line represents the frontier for the necessary condition (4.18): blockage may arise whenever the colloids cross this line. As seen in figures 15(a), 15(c) and 15(e), this situation arises for all three values of the temperature difference. Indeed, when looking at the corresponding averaged profiles $\langle x\rangle_c(t)$ (figure 15b,d,f), we observe a small decrease at short times, associated with a short blockage. However, only in the third experiment, corresponding to the largest temperature difference, does the blockage last in the long term, showing an approximately constant mean profile $\langle x\rangle_c(t)$.

This can be explained by calculating the velocity drift v_m (salt attraction) in the salt-in configuration. Using (4.5) with $i = 1$, we obtain

$$v_m(x,\,t) \sim D_{dp}\sqrt{Pe_s}\,\frac{x}{\langle x^2\rangle_s(t)} \underset{t\to 0}{\sim} D_{dp}\sqrt{Pe_s}\,\frac{x}{\langle x^2\rangle_s(0)}. \tag{4.19}$$

Therefore, at short time, the salt attraction is more important at higher Péclet number. On the other hand, the common transport (reference case) is approximately independent of the Péclet number, as seen in § 3.3. Since the colloids will get more blocked if they remain long enough in their cell, the blockage is more likely to happen when the transient salt effect is strong enough to cancel the common transport, and therefore more probable at a larger Péclet number.

Finally, note that when colloids are blocked, even though the blockage condition (4.18) is no longer satisfied (see figure 14), they remain blocked until diffusion has had time to bring them near the walls again. Looking at figure 16, which shows a snapshot of the experiment when blockage is reached, with the small diffusion coefficient of the colloids, it can clearly take a long time, which explains why the quantity $\langle x\rangle_c(t)$ in figure 15(f) remains approximately constant for so long.

5. Summary and conclusion

We have studied experimentally the joint transport of salt and colloids in a steady Rayleigh–Bénard flow composed of an alignment of steady convection rolls in a closed horizontal chamber. By means of high dynamical range light-induced fluorescence, we have measured the instantaneous concentration fields of colloids and salt to address how they are transported at long times. In such a configuration, we recover diffusive-like transport at long time for the salt (Shraiman 1987; Soward 1987; Solomon & Gollub 1988*b*; Young *et al.* 1989): after a long transient following injection of salt on one side of the chamber, the coarse-grained salt concentration profile reaches a Gaussian shape at large scale, and spreads with a diffusive scaling, with sharp gradients located between convection cells. Note that we do not recover diffusive-like dispersion in the case of colloids alone (without salt) due to their interaction with the metallic walls, an effect that was found to be nearly independent of the Péclet number.

https://doi.org/10.1017/jfm.2025.10813 Published online by Cambridge University Press

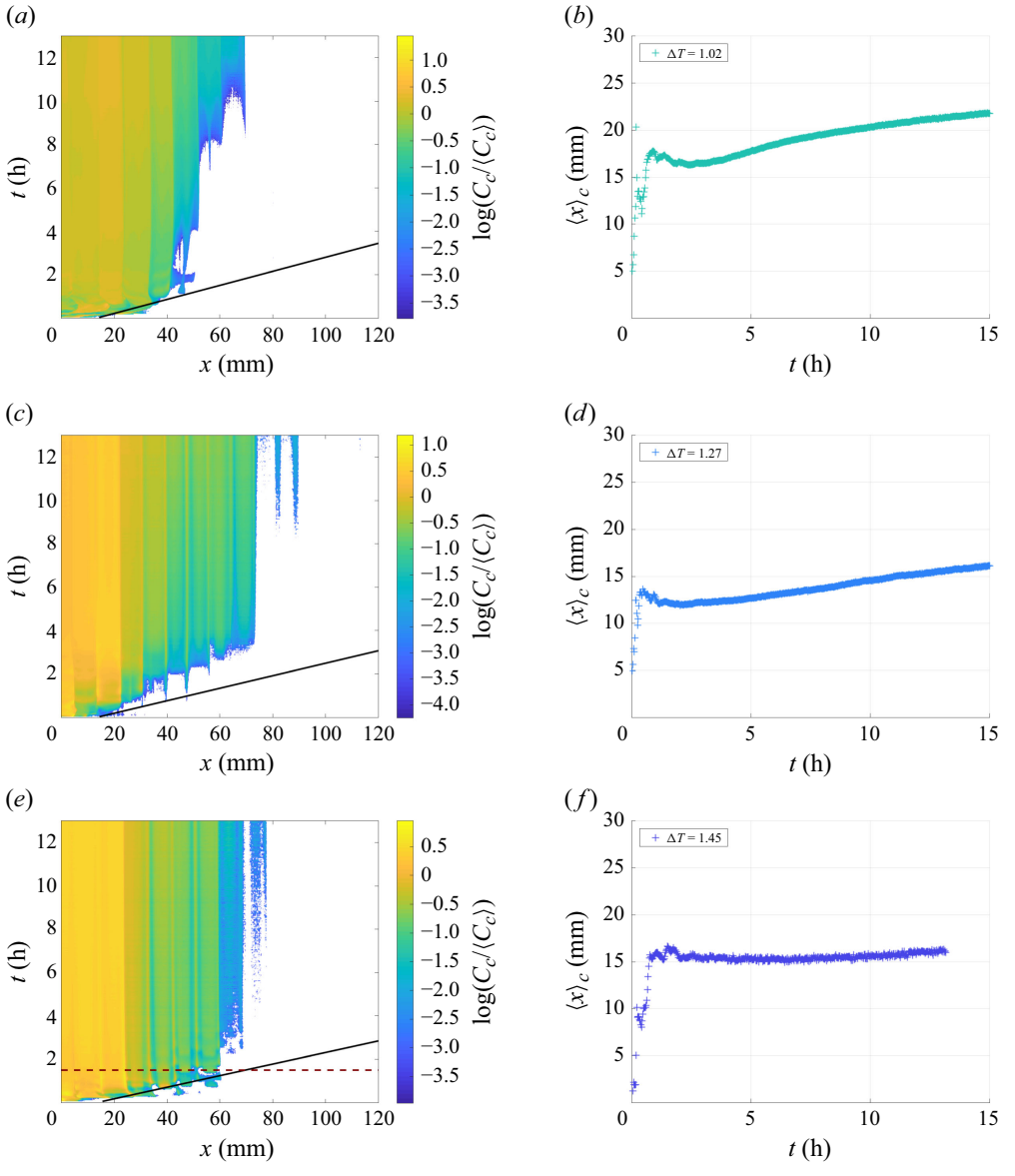


Figure 15. Salt-in configuration. (*a*,*c*,*e*) Normalised concentration profiles in x, together with (*b*,*d*,*f*) their average position $\langle x\rangle_c(t)$, for three different values of the temperature difference ΔT, increasing from top to bottom: (*a*,*b*) $\Delta T = 1.02\,^{\circ}\mathrm{C}$, (*c*,*d*) $\Delta T = 1.26\,^{\circ}\mathrm{C}$, (*e*,*f*) $\Delta T = 1.45\,^{\circ}\mathrm{C}$. The solid line has equation $x = 1.43\,\langle x^2\rangle_s(t)/L$ (from (4.18)), with $L = 9.4$ mm and $\langle x^2\rangle_s(t) \approx 9.4^2 + 13\times 10^{-4}\sqrt{Pe_s t}$ (from (3.6)). Blockage may happen whenever the profile crosses this line (necessary condition). From the mean profiles $\langle x^2\rangle_c(t)$ in (*b*,*d*,*f*), it is visible that blockage lasts the longest for the largest temperature difference ΔT (largest Péclet number). The dashed line in (*e*) at time $t = 1.5$ h is the time corresponding to the snapshot of figure 16.



Figure 16. Blockage situation for $\Delta T = 1.45\ ^{\circ}\mathrm{C}$ and $t = 5400\ \mathrm{s} = 1.5$ h (dashed line in figure 15*e*). The coefficient R increases from left to right, following (4.17).

https://doi.org/10.1017/jfm.2025.10813 Published online by Cambridge University Press

In order to address the influence of the salt gradients on colloid transport, and test the theoretical predictions derived in Volk *et al.* (2022), we have tested two configurations, which were compared to the reference case of colloid transport without diffusiophoresis.

In the salt-out configuration, for which colloids and salt are injected at both ends of the chamber with a tunable time delay, the salt gradient is moderate, and the blockage criterion adapted from Volk *et al.* (2022) is rather low. We find that the transport of colloids is enhanced as compared to the reference case, as predicted in the theoretical work. Moreover, we obtain a qualitative agreement between the measured spreading rate of the colloids at intermediate times and estimations derived, assuming that the coarse-grained salt concentration is Gaussian at large scale, and scaling laws derived in Volk *et al.* (2022) can be transposed to the present situation. However, the prediction based on diffusiophoresis falls off in the long-time regime since this effect can be only transient in a cell of finite size.

In the salt-in configuration, for which colloids and salt are injected together in the chamber, strong phoretic effects can occur at short time as salt has not entirely spread over the chamber. For the three increasing values of the colloids Péclet number, we observe a transient blockage of the colloids in convection cells; the longer the trapping, the larger the Péclet number. The occurrence of such trapping is found in agreement with the threshold for blockage derived from the salt profile; increasing the Péclet number enhances the transient salt attraction, and can annihilate the effect of the second mechanism (colloids attracted by the horizontal walls), which plays against blockage.

Although the results obtained in Volk *et al.* (2022) were derived with strong hypotheses (constant gradient, stationary regime, linear velocity drift), the theory proved to give satisfactory predictions in the present experimental case for which none of these hypotheses were strictly holding. This shows that scale separation, whether in time or space, and the precise nature of the phoretic mechanism are less important than the topology of the flow (with closed streamlines) to observe the regimes of enhanced transport or blockage. As a consequence, the present results and analysis should hold in a large variety of transport phenomena, e.g. transport of living cells in cellular flows under the influence of chemotaxis.

Funding. This work was supported by the French research programmes ANR-16-CE30-0028. For the purpose of Open Access, a CC-BY public copyright licence has been applied by the authors to the present manuscript and will be applied to all subsequent versions up to the Author Accepted Manuscript arising from this submission.

Declaration of interests. The authors report no conflict of interest.

References

Abécassis, B., Cottin-Bizonne, C., Ybert, C., Ajdari, A. & Bocquet, L. 2009 Osmotic manipulation of particles for microfluidic applications. *New J. Phys.* **11** (7), 075022.

Anderson, J.L. 1989 Colloid transport by interfacial forces. *Annu. Rev. Fluid Mech.* **21**, 61–99.

Ault, J.T. & Shin, S. 2025 Physicochemical hydrodynamics of particle diffusiophoresis driven by chemical gradients. *Annu. Rev. Fluid Mech.* **57**, 227–255.

Bergougnoux, L., Bouchet, G., Lopez, D. & Guazzelli, E. 2014 The motion of solid spherical particles falling in a cellular flow field at low Stokes number. *Phys. Fluids* **26** (9), 093302.

Chu, H.C.W., Garoff, S., Tilton, R.D. & Khair, A.S. 2020 Advective–diffusive spreading of diffusiophoretic colloids under transient solute gradients. *Soft Matter* **16** (1), 238–246.

Chu, H.C.W., Garoff, S., Tilton, R.D. & Khair, A.S. 2021 Macrotransport theory for diffusiophoretic colloids and chemotactic microorganisms. *J. Fluid Mech.* **917**, A52.

Chu, H.C.W., Garoff, S., Tilton, R.D. & Khair, A. 2022 Tuning chemotactic and diffusiophoretic spreading via hydrodynamic flows. *Soft Matter* **18**, 1896–1910.

https://doi.org/10.1017/jfm.2025.10813 Published online by Cambridge University Press

CUI, H., LIN, Z., ZHU, K., CHENG, G., WU, X. & ZHENG, R. 2024 Effect of surface corrosion on the zeta potential of copper in acidic solutions. *Surf. Interfaces* **54**, 105291.

DERJAGUIN, B.V., DUKHIN, S.S. & KOROTKOVA, A.A. 1961 Diffusiophoresis in electrolyte solutions and its role in the mechanism of the formation of films from caoutchouc latexes by the ionic deposition method. *Colloid J. USSR* **23**, 53–58.

DESEIGNE, J., COTTIN-BIZONNE, C., STROOCK, A.D., BOCQUET, L. & YBERT, C. 2014 How a 'pinch of salt' can tune chaotic mixing of colloidal suspensions. *Soft Matter* **10**, 4795–4799.

GUPTA, A., SHIM, S. & STONE, H.A. 2020 Diffusiophoresis: from dilute to concentrated electrolytes. *Soft Matter* **16** (30), 6975–6984.

GUYON, E., POMEAU, Y., HULIN, J.P. & BAUDET, C. 1987 Dispersion in the presence of recirculation zones. *Nucl. Phys. B: Proc. Suppl.* **2**, 271–280.

LEE, S., LEE, J. & AULT, J.T. 2023 The role of variable zeta potential on diffusiophoretic and diffusioosmotic transport. *Colloids Surf. A: Physicochem. Engng Aspects* **659**, 130775.

MAUGER, C., VOLK, R., MACHICOANE, N., BOURGOIN, M., COTTIN-BIZONNE, C., YBERT, C. & RAYNAL, F. 2016 Diffusiophoresis at the macroscale. *Phys. Rev. Fluids* **1**, 034001.

MOFFATT, H.K. 1983 Transport effects associated with turbulence with particular attention to the influence of helicity. *Rep. Prog. Phys.* **46** (5), 621.

POMEAU, Y. 1985 Dispersion dans un écoulement en présence de zones de recirculation. *C. R. Acad. Sci. Paris II* **301** (19), 1323–1326.

PRIEVE, D.C., ANDERSON, J.L., EBEL, J.P. & LOWELL, M.E. 1984 Motion of a particle generated by chemical gradients. Part 2. Electrolytes. *J. Fluid Mech.* **148**, 247–269.

RAYNAL, F., BOURGOIN, M., COTTIN-BIZONNE, C., YBERT, C. & VOLK, R. 2018 Advection and diffusion in a chemically induced compressible flow. *J. Fluid Mech.* **847**, 228–243.

RAYNAL, F. & VOLK, R. 2019 Diffusiophoresis, Batchelor scale and effective Péclet numbers. *J. Fluid Mech.* **876**, 818–829.

RENAUD, A. & VANNESTE, J. 2020 Dispersion of inertial particles in cellular flows in the small-Stokes, large-Péclet regime. *J. Fluid Mech.* **903**, A2.

SARVER, E., SLABAUGH, R., STROCK, C. & EDWARDS, M. 2016 Flow electrification and non-uniform corrosion in low conductivity potable waters. *J. Electrochem. Soc.* **163** (5), C139.

SHRAIMAN, B.I. 1987 Diffusive transport in a Rayleigh–Bénard convection cell. *Phys. Rev. A* **36** (1), 261.

SOLOMON, T.H. & GOLLUB, J.P. 1988*a* Chaotic particle transport in time dependent Rayleigh–Bénard convection. *Phys. Rev. A* **38** (12), 6280–6286.

SOLOMON, T.H. & GOLLUB, J.P. 1988*b* Passive transport in steady Rayleigh–Bénard convection. *Phys. Fluids* **31** (6), 1372–1379.

SOWARD, A.M. 1987 Fast dynamo action in a steady flow. *J. Fluid Mech.* **180**, 267–295.

SWINEHART, D.F. 1962 The Beer–Lambert law. *J. Chem. Educ.* **39** (7), 333.

VOLK, R., BOURGOIN, M., BRÉHIER, C.-É. & RAYNAL, F. 2022 Phoresis in cellular flows: from enhanced dispersion to blockage. *J. Fluid Mech.* **948**, A42.

VOLK, R., MAUGER, C., BOURGOIN, M., COTTIN-BIZONNE, C., YBERT, C. & RAYNAL, F. 2014 Chaotic mixing in effective compressible flows. *Phys. Rev. E* **90**, 013027.

WANG, F. 2018 Linearity research of a CMOS image sensor. PhD thesis, Delft University of Technology.

YOUNG, W., PUMIR, A. & POMEAU, Y. 1989 Anomalous diffusion of tracer in convection rolls. *Phys. Fluids A: Fluid Dyn.* **1** (3), 462–469.

https://doi.org/10.1017/jfm.2025.10813 Published online by Cambridge University Press